Multiwave inversion: A key step for depth model building — Examples from the Sultanate of Oman

Daniela Donno[1], Mohammad Sheryar Farooqui[1], Mostafa Khalil[1], David McCarthy[1], Didier Solyga[2], Jillian Courbin[2], Anthony Prescott[2], Laurie Delmas[2], and David Le Meur[2]

https://doi.org/10.1190/tle40080610.1

Abstract

The near surface in the Middle East, particularly in the Sultanate of Oman, is characterized by very shallow high-velocity carbonates and anhydrites interleaved by slow-velocity clastic layers, resulting in sharp velocity inversions in the first few hundred meters below the surface. In addition, the surface is characterized by features such as unconsolidated materials within dry riverbeds (known as "wadis"), small jebels, and sand dunes, which cause distortions in the underlying shallow and deeper seismic images. This work presents the building of a near-surface model by using multiwave inversion that jointly inverts information from P-wave first breaks and surface-wave dispersion curves. The use of surface waves in combination with first breaks captures the lateral and vertical velocity variations, especially in the shallowest parts of the near surface. This paper focuses on the analysis of two drawbacks of this technology: the picking of the input data information, which can be cumbersome and time consuming, and the limited penetration depth of surface waves at the typical frequencies of active data. To overcome these issues, an innovative workflow is proposed that combines the use of an unsupervised machine learning technique to guide the pick extraction phase and the reconstruction of ultra-low-frequency surface waves (0.5 to 1.5 Hz) through an interferometry process using information from natural and ambient noise. Deeper near-surface P- and S-wave velocity models can be obtained with multiwave inversion using these ultra-low frequencies. The integration of a near-surface model into the velocity model building workflow brings a major improvement in depth imaging from shallow to deep structures, as demonstrated on two data sets from the Sultanate of Oman.

Introduction

The near surface in the Arabian Peninsula, particularly in the Sultanate of Oman, is characterized by complex geologic features such as shallow anhydrite layers and carbonate sequences with high velocities overlying lower-velocity clastic series (Forbes et al., 2010). This geologic sequence yields shallow sharp velocity inversions, causing seismic imaging to be challenging. Accurately capturing these shallow velocity inversions during model building is necessary to image both shallow and deep targets and to minimize image distortions and migration artifacts. Estimation of the P-wave velocity (V_P) model for the first kilometer below the surface can be difficult due to rapid vertical and lateral variations in the geologic structures. Despite some major advances in depth imaging technology based on full-waveform inversion (FWI) (Stopin et al., 2013; Sedova et al., 2017; Perez Solano and Plessix, 2019), the imprint caused by the near surface remains a major challenge for land depth imaging.

Over the last decades, approaches based on refracted P-waves, such as first-arrival traveltime tomography (Taillandier et al., 2009), have been the standard methods for creating velocity models of the near surface. However, first-arrival traveltime tomography usually lacks resolution in the shallow part of the medium due to the horizontal nature of diving waves and their inability to capture small and rapid velocity inversions, mainly due to shingling effects (Golikov and Bakulin, 2014). In order to overcome this issue, surface-wave inversion has emerged as an alternative solution (Socco and Strobbia, 2004; Boiero et al., 2013). Surface waves are very sensitive to lateral and vertical velocity variations, especially in the shallowest parts of the near surface. They provide S-wave velocity (V_S) information that needs to be converted into a V_P velocity field for depth imaging. Moreover, joint inversion algorithms have been proposed using different seismic input data, such as first breaks and surface-wave dispersion curves (Dal Moro and Pipan, 2007; Re et al., 2010), or nonseismic data (Colombo et al., 2008). The advantage of joint inversions lies in the merging of different information, which decreases the ill-posed nature of the inversion and leads to more reliable solutions.

In this paper, we create near-surface velocity models by using multiwave inversion (MWI) (Bardainne, 2018), which jointly inverts first breaks, surface-wave dispersion curves, and vertical two-way traveltimes using a stochastic inversion approach. We focus our analysis on methods to overcome two drawbacks of this technology: the picking of the input data information, which can be cumbersome and time consuming, and the limited penetration depth of surface waves at the typical frequencies of active data. First, we show how unsupervised machine learning (ML) can be crucial to recovering the accuracy of surface-wave velocity picking (Hou et al., 2019). We present an automated ML dispersion-curve-picking flow to improve picking reliability on both low and high frequencies of the phase-velocity spectra and demonstrate its impact on MWI results. Second, because the penetration depth of surface waves depends on the minimum recorded frequency, the depth of an MWI-inverted velocity model is limited to a few hundred meters for conventional seismic data with minimum reliable frequencies of approximately 2 Hz. To overcome this constraint, we propose using passive surface waves reconstructed by interferometry of blended continuous-recording data (Le Meur et al., 2020). The continuous-recording data contain lower frequencies from natural sources (e.g., ocean waves, wind, and microearthquakes) and human

[1]CGG, Muscat, Oman. E-mail: daniela.donno@cgg.com; mohammad.farooqui@cgg.com; mostafa.khalil@cgg.com; david.mccarthy@cgg.com.
[2]CGG, Massy, France. E-mail: didier.solyga@cgg.com; jillian.courbin@cgg.com; anthony.prescott@cgg.com; laurie.delmas@cgg.com; david.lemeur@cgg.com.

activity than those emitted by active seismic sources. The interferometry method allows us to use this seismic noise to reconstruct passive virtual data characterized by ultra-low frequencies (Schuster, 2009). As recently shown by Dellinger and Yu (2009) and Brenguier et al. (2019), ultra-low-frequency passive seismic data can successfully image much deeper structures.

We show the benefit of applying all of these techniques on two case studies from the Sultanate of Oman (one from the north and one from the south; Figure 1). First, we demonstrate the efficiency of the unsupervised ML workflow for improving surface-wave picking. Second, we apply the seismic interferometry approach to retrieve ultra-low-frequency surface waves. Our results prove that these technologies better characterize the near surface and have a significant positive impact on the imaging of deeper events.

Figure 1. Satellite map of the Sultanate of Oman showing the locations of the two study areas in the north and south (red squares).

Challenges of reliable surface-wave and first-break picks

The success of MWI strongly depends on the quality of picking the first breaks and surface-wave dispersion curves. In this section, we analyze the challenges of obtaining reliable surface-wave and first-break picks and how the use of ML tools can help with these tasks. We present our workflow on a data set from the southern part of the Sultanate of Oman (bottom red square in Figure 1). The velocity variations in this area are illustrated in Figure 2a, where the phase velocity of the surface phase extracted at a fixed frequency (8 Hz) shows lower-velocity areas (corresponding to basins and wadis) surrounded by higher velocities in the gravel plain. Wave propagation in such a laterally variable near surface affects the seismic arrivals. This is illustrated in Figure 2b (yellow arrow), which shows distortions of both shallow and deeper seismic reflections below the wadi.

For inversion of the surface-wave velocity, it is important to pick the phase velocity on a reliable surface-wave propagation mode, such as the fundamental mode. In order to avoid the picking of higher overtones, we must constrain the surface-wave velocity picking within a predefined velocity/frequency corridor. However, due to the spatially varying nature of the phase velocity, as shown in Figure 2a, defining one single a priori velocity/frequency corridor for the whole survey is not appropriate. To capture the large spatial and frequency-dependent velocity variations, the creation of a robust guide is necessary. This is computed from the dispersion panels. To ease this task, we built a workflow that employs an unsupervised ML technique to select the smallest number of relevant dispersion panels describing the characteristics of the surface waves required for the inversion (Masclet et al., 2019). Before detailing the ML-guided corridor workflow, we need to improve the signal-to-noise ratio of the data used for picking. Aliasing of surface waves and other coherent/random noise due to survey acquisition or in-field facilities can significantly affect the quality and interpretation of the dispersion panels. Therefore, rigorous preconditioning is applied, including several denoising techniques such as a low-rank sparse inversion (Sternfels et al., 2015) to remove noncoherent noise and a data-driven interferometry approach (Chiffot et al., 2017) to interpolate the surface waves and remove aliased events. The benefit of this processing sequence is shown in Figure 3 with the input and conditioned gathers from two different locations (corresponding to the blue and yellow stars in Figure 2a). The seismic gather located in the wadi area (top of Figure 3) shows strong phase-velocity variations from low to high frequencies (400 m/s at 25 Hz). Instead, for the gather in the gravel plain (bottom of Figure 3), the dispersion of surface waves is lower with higher velocities at high frequencies

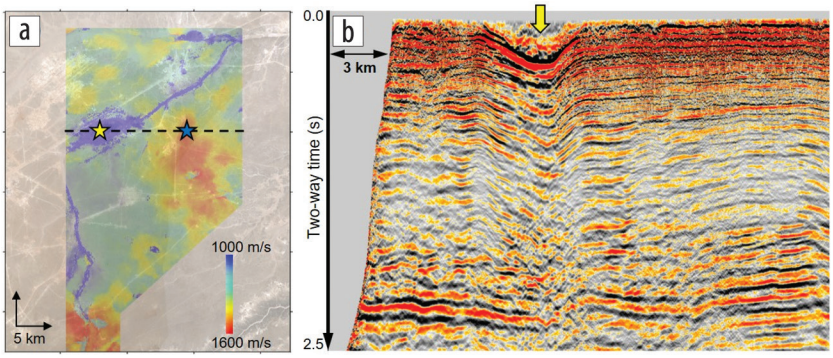

Figure 2. (a) Overlay of the satellite map with the phase velocity extracted from the surface waves at 8 Hz. The two stars indicate the location of the shot gathers shown in Figure 3. (b) Seismic section in time through the wadi and gravel plain, corresponding to the black dashed line in (a). The yellow arrow indicates the wadi location.

(1200 m/s at 25 Hz) and several velocity inversions visible below 5 Hz. Our preconditioning flow also reveals improved continuity of the dispersion curves on the lower frequencies, thus allowing an increase in the maximum depth of the velocity model from MWI.

After this preprocessing, the dispersion panels are clustered using an unsupervised ML method based on K-means clustering (MacQueen, 1967), such that dispersion panels belonging to a cluster are more similar to each other than to those in other clusters. For this survey, K-means clustering with 20 clusters is applied to all dispersion panels. During this process, a centroid image is created for each cluster corresponding to the most representative dispersion panel for each cluster. Among the created clusters, those corresponding to centroid images with inconsistent dispersion-curve shapes, as shown in Figure 4b, are interpreted by the user as outliers and rejected. These outliers are mainly located at the edges of the survey or correspond to very noisy or incomplete input data. Only the clusters that correspond to good-quality dispersion panels are kept by checking their spatial distribution and consistency with the centroid panel. For this data set, eight clusters are selected, as shown in Figure 4a. From this figure, it is observed that the clustering map of the selected clusters reveals good correlation with geologic features, such that the dispersion curves related to wadis and other low-velocity areas can be accurately separated from the rest of the data. Another important parameter from K-means clustering that can be used to perform quality control of the dispersion panels is the Euclidian distance measured between each dispersion panel and its associated centroid for each cluster (Figure 5). This distance describes the consistency and similarity of dispersion panels within the same cluster. Panels with small Euclidian distance values resemble the centroid panel, while those with higher distances are characterized by distorted modes. For each selected cluster, poor-quality panels were discarded based on their Euclidian distance from the centroid

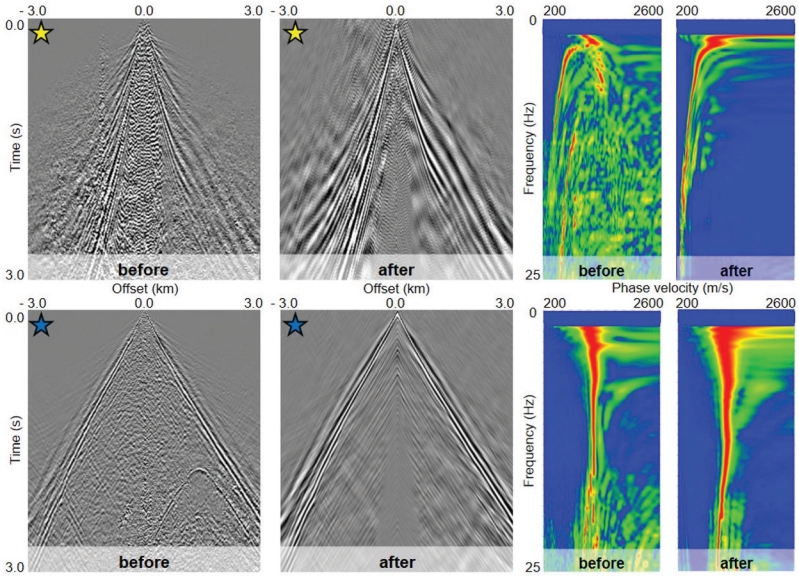

Figure 3. Input (left) and processed (center) shot gathers and their associated dispersion curves (right) computed over a spatial window of 1 km offset. Top: the wadi area (yellow star in Figure 2a). Bottom: the gravel plain (blue star in Figure 2a).

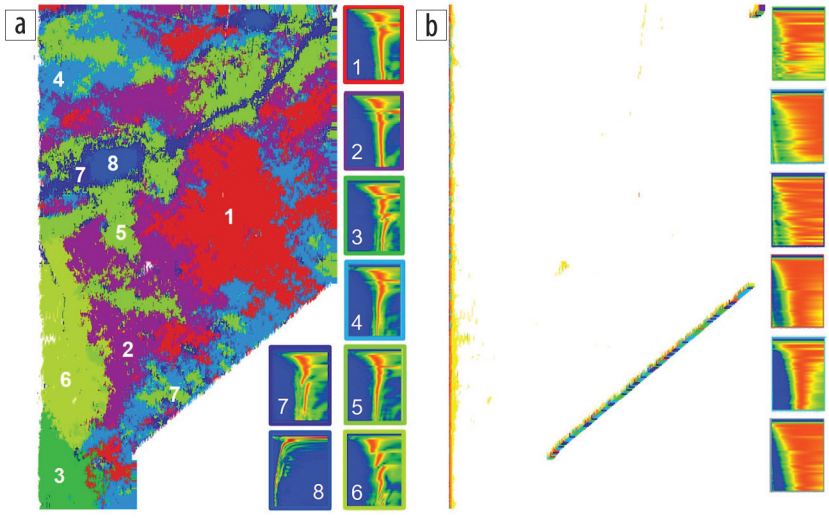

Figure 4. K-means clustering maps. (a) Locations kept with the selected eight clusters (red to blue colors). (b) Locations of outlier clusters corresponding to survey edges or noisy locations.

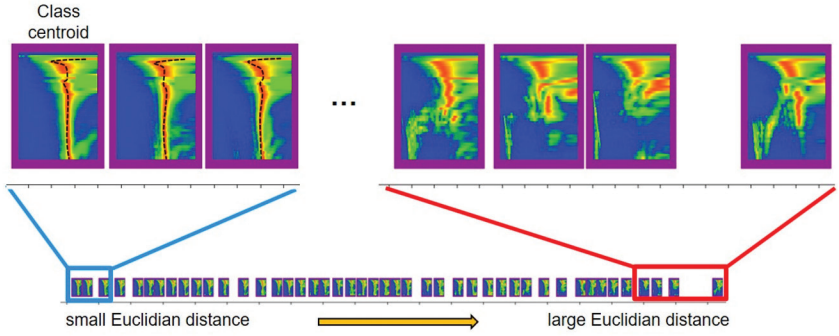

Figure 5. Euclidian distance plot for cluster 2. Dispersion panels at the farthest distance from the centroid image correspond to low-quality panels and are therefore discarded. Here, only a percentage of panels within a defined standard deviation are kept and picked based on maximum amplitude in order to extract a guide (dashed black lines).

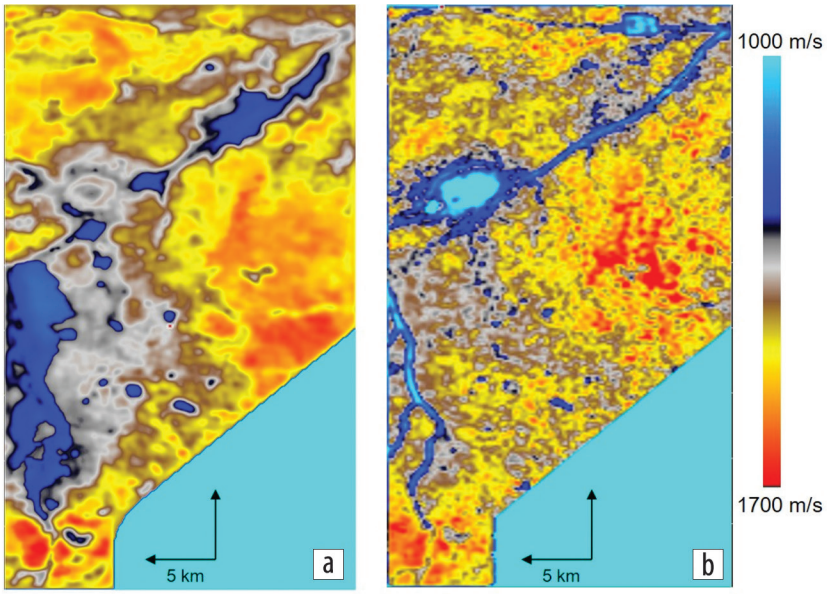

Figure 6. Frequency slice at 8 Hz after the surface-wave tomography with (a) manually defined polygons to create different picking corridors for the low- and high-velocity areas and (b) the described unsupervised ML workflow. Low-velocity anomalies correlate well with the wadi contour observed on the satellite map (Figure 2a) and on the shallow depth seismic sections (Figures 7a and 7b).

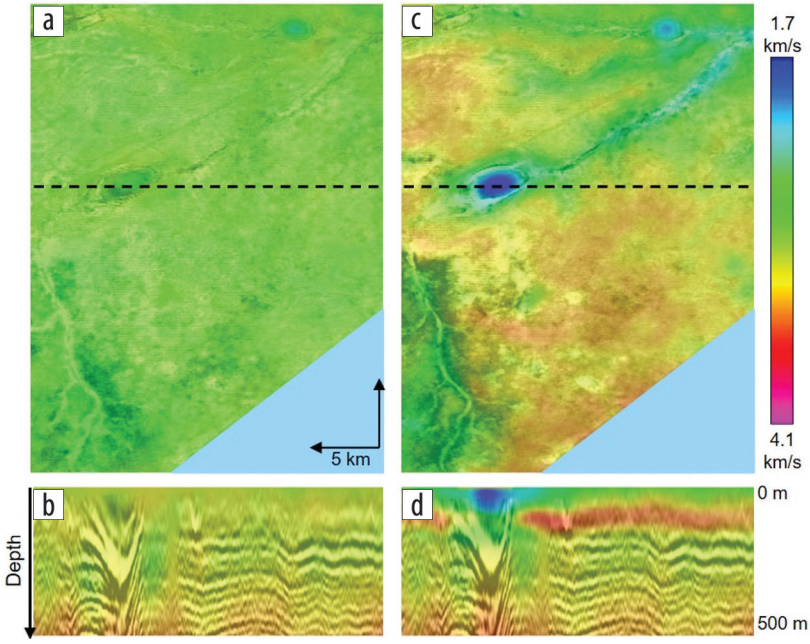

Figure 7. V_P velocity model overlaid on migrated seismic (a–b) from first-break tomography and (c–d) from MWI. Top: Depth slices at 70 m below the topography. Bottom: Near-surface migrated section located along the dashed black line. The maximum depth penetration of the MWI is related to the minimum picked frequency. It is about 200 m below the topography in this example.

according to a standard deviation value chosen by the user after overall analysis of the clusters. Generally, about 90% of the panels are kept within each cluster. A frequency-dependent velocity corridor is then automatically picked on all selected panels by selecting the maximum amplitude of the dispersion curves at each frequency (dashed lines on the panels in Figure 5). The guide is spatially interpolated and filtered for the whole survey and used as an adequate corridor in frequency or period versus the phase velocity for the picking on all panels (Bouhdiche et al., 2020). The picking method (Duret et al., 2016) consists of a multiazimuth 3D extension of the multioffset phase analysis technique proposed by Strobbia and Foti (2006). For each gather, traveltime picks are estimated not only for every frequency/period but also for different azimuth directions in order to obtain higher lateral resolution for the subsequent surface-wave tomography. This step converts the spatially irregular frequency-dependent picks into a regularized (x, y, frequency/period) Rayleigh wave velocity volume (Figure 6). Figure 6a shows the surface-wave tomography result obtained with manually defined polygons to create different picking corridors for the low- and high-velocity areas. Figure 6b shows the result obtained after using the described ML workflow. The tomographic result using ML-guided picking contains more structural detail and clearly identifies wadis and other slow-velocity anomalies.

In addition to surface-wave picks, first-break picks are also used in MWI. A quality-control step is necessary to remove outliers or picks with cycle skips. K-means clustering was used to build a velocity corridor in the velocity/offset domain in order to edit out the first-break picks associated with a velocity inversion or anomalous values, especially at near and far offsets (Prieux et al., 2020). Finally, the selected first-break picks and the regularized Rayleigh wave velocity volume are jointly inverted to provide V_P and V_S near-surface velocity fields. Figure 7 shows a comparison of the P-wave velocity model obtained with MWI (Figures 7c and 7d) and with first-break tomography alone (Figures 7a and 7b). The V_P model updated by MWI successfully captures the sharp lateral velocity variations around the wadi, as well as the first velocity increase below the topography (Figure 7d), which corresponds to the Taqa Formation. However, in order to capture deeper velocity inversions (beyond the 200 m depth of the actual MWI model), we need Rayleigh waves with frequencies lower than those recorded on the active seismic. Here, the minimum frequency of the vibrator sweep started at 1.5 Hz. To reconstruct

ultra-low-frequency surface waves, we use an interferometry process by utilizing natural and ambient noise, as described in the next section.

Recovering ultra-low-frequency surface waves from interferometry of continuous recordings

With the increasing deployment of blended land acquisition surveys (Abma et al., 2015) based on continuous recording, there is an opportunity to reconstruct ultra-low-frequency surface waves through an interferometry process with natural and ambient noise (Le Meur et al., 2020; Al-Droushi et al., 2021). Blended continuous-recording surveys have become increasingly common for land acquisition in desert environments in recent years (Zhao et al., 2018) because they reduce the cost of broadband wide-azimuth acquisitions. The recording periods without active sources are not seismically quiet because sources generating ambient and natural noise are always present in the background. Moreover, while the useful frequency range for active data is limited by the minimum frequency of the source sweep (generally 1.5 or 2 Hz for modern acquisitions), seismic signals created by natural sources (e.g., ocean waves) or human activity cover a lower frequency range, down to about 1 Hz for human activity and well below this limit for natural noise (Boué et al., 2019). During blended land acquisitions, all of these seismic signals/noise sources are recorded for several days or weeks.

The interferometry method (Wapenaar, 2004) allows us to use continuous-recording seismic to reconstruct passive virtual data, such as surface or refracted waves. Seismic interferometry utilizes the cross correlations of seismic traces to reconstruct the Green's function between the receivers. From a practical point of view, we divide the continuous data into time intervals (e.g., every 30 s) to form subsets of gathers for the interferometry computation. For each subset, a virtual source position is defined, and the closest receiver station to the chosen virtual source position is cross correlated with all other stations in the same subset. All virtual shots from all time intervals are then stacked to form the final virtual shot. Usually, the main constructive contributions to interferometry come from noise sources located within stationary phase areas (Snieder, 2004). The locations of the vibrated points and the sweep emission times of blended acquisition enable us to relate the time intervals of continuous records to the noise sources coming from these stationary phase areas. Then, the noise sources within a given angular direction are selected by excluding the simultaneous vibrated points, which are too close to the selected receiver stations. This enables better reconstruction of the virtual shot and prevents a large bias from the active blended data.

We reconstructed 2D virtual shot gathers (over a 300 × 300 m grid) by interferometry on the same study area from the southern part of the Sultanate of Oman by using data with 15 days of continuous recordings. Surface Rayleigh waves are the main type of reconstructed waves because their propagation is linear between receivers and they are the highest-energy seismic waves propagating in desert environments. By comparing virtual shots computed at selected locations with active deblended shots at the same locations, we can observe that the propagation of surface waves is well reconstructed (Figures 8a and 8d). The selected virtual shot gather is at the boundary between the wadi area and the gravel plain (close to the position of the shot gather in Figure 3a [yellow star]). We can observe that the surface-wave properties are different for the positive and negative offsets, as shown by the dispersion-curve gathers for the negative offsets (Figures 8b and 8e) and the positive offsets (Figures 8c and 8f), which present different phase-velocity values for a given frequency. Moreover, we notice that the virtual shot contains lower frequencies with higher signal-to-noise ratio than the active one. This indicates that the picking of the maximum of the dispersion curve is more accurate and robust on the fundamental mode. Finally, dispersion panels show that the minimum usable frequency is 1.5 Hz for the active shot (which is the starting frequency of the vibrator sweep) and 0.5 Hz for the virtual shot. We therefore expect that if we invert the surface waves from virtual shots, the investigation depth will triple because the penetration depth of surface waves is inversely proportional to the minimum recorded frequency (Socco and Strobbia, 2004). In the next two sections, we apply the workflow described earlier to two data sets from the south and the north of the Sultanate of Oman.

Case study from the south of the Sultanate of Oman

The near-surface geology in this area is composed of complex interleaved low- and high-velocity layers (with V_P from 2000 to 4500 m/s), such as shale/sandstone and carbonates, which also vary in thickness from a few tens to hundreds of meters. Moreover, the topography is characterized by wadis and gravel plains. For MWI, we used the surface-wave dispersion curves extracted from active deblended and virtual data and combined them with first-break picks. The ML-based corridor was used to enable the picking as described. For this survey, the frequency range for dispersion-curve picking was from 1.5 to 15 Hz on the active data and from 0.5 to 9 Hz on the virtual shots. For layering of the initial velocity models, we used layers that follow the main geologic structures, which helped the inversion to spatially follow the geologic variation trend of the near surface. We used thinner layers (about 10 m) in the shallow part and thicker layers in the deeper part (about 50–60 m), according to the expected resolution of the surface waves. Figure 9 shows the V_P velocity models inverted with MWI using either the active dispersion curves (Figure 9b) or the active and virtual ones together (Figure 9c). The near-surface models were merged with the legacy ray-based tomography model (Figure 9a). The maximum depth of the model inverted with virtual data is about 700 m (Figure 9c), which is significantly deeper than the 200 m depth achieved with active data (Figures 7d and 9b). This near-surface MWI model also shows a good fit with the sonic log (Figure 9d) for the first 700 m below the surface, which is approximately the maximum penetration depth of surface waves. From the comparison between the sonic log and the V_P profile from MWI, we observe that while the shallower high-velocity layer can be obtained using either the active or virtual data (yellow and green curves, respectively), the deeper velocity variations with the alternating slow and fast velocities are only recoverable by the inversion with virtual surface-wave data (green curve).

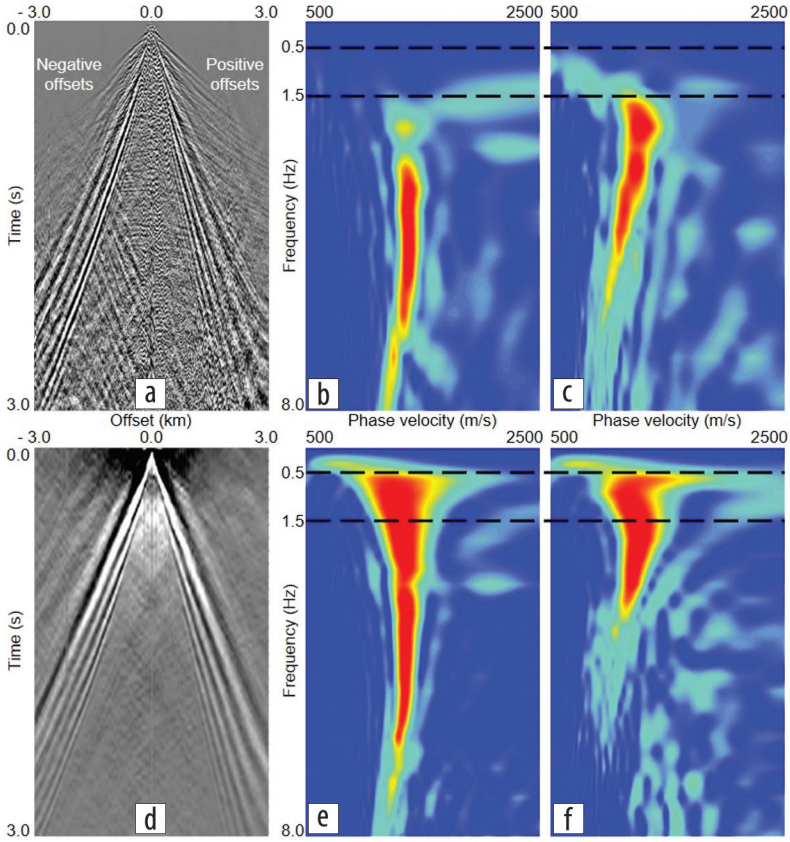

Figure 8. (a) Active shot with its dispersion panels using (b) the negative offsets and (c) the positive offsets. (d) Virtual passive shot with its dispersion panels using (e) the negative offsets and (f) the positive offsets. The low frequencies of the virtual shot have a higher signal-to-noise ratio than the active one. The picking of the maximum of the dispersion curve is therefore more accurate and robust on the fundamental mode.

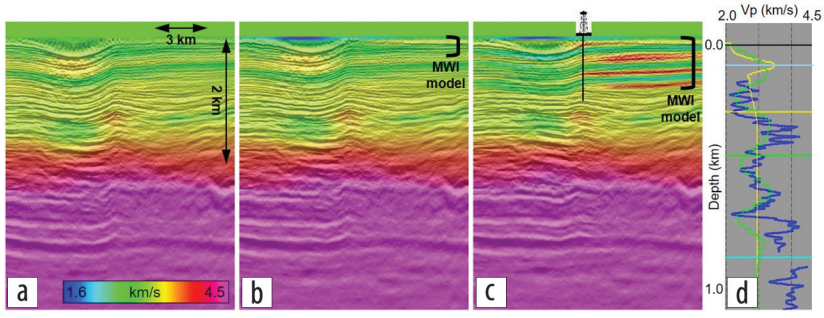

Figure 9. Kirchhoff depth-migrated sections overlaid by the velocity model using (a) legacy tomography-based velocity model without MWI, (b) MWI model from active data merged with the legacy model, and (c) MWI model from active and virtual data merged with the legacy model. (d) Sonic log (blue) with the main lithostratigraphy formations overlaid by the V_P velocity profiles from the MWI with active data (yellow) and active and virtual data (green). Courtesy Le Meur et al. (2020).

The influence of near-surface velocity models on depth imaging is confirmed by Kirchhoff depth migration with the velocity models shown in Figure 9. The MWI models are merged with the legacy tomography-based velocity model beyond their maximum penetration depth in order to obtain the full velocity model from top to bottom. Compared to the depth-migrated image obtained with the legacy tomography velocity model (Figure 10a), the depth section with the V_P near-surface model inverted from active data down to 200 m below the topography shows only small improvements under the wadi and in the deeper parts (Figure 10b). Instead, major improvements are visible on the shallow and deep structural image when the near-surface V_P model is replaced (down to about 700 m below the surface) with the MWI model inverted from both virtual and active data (Figure 10c). The green arrows show better focusing and simpler structures below the wadi. Moreover, the yellow arrows and dashed rectangles highlight areas of the presalt Nafun Group (between 2.5 and 4 km depth), where the structure is distorted when the legacy tomography-based velocity model (Figure 10a) is used for imaging. The focusing of the deep Nafun structure is improved when the deeper near-surface MWI model is included in the depth velocity model (Figure 10c). The depth slice at 3.6 km also reveals that the shallower structures in the wadi area (within the yellow circle in Figure 10d) show an imprint on the deep presalt layers. The use of MWI near-surface models (Figures 10e and 10f) significantly improves focusing and lateral consistency of these deeper presalt events and removes the imprint of the shallow structures.

Case study from the north of the Sultanate of Oman

This area is characterized by a very complex near surface, exposing a thrust-faulted antiform structure with steeply dipping flanks going right up to the surface. These fault flanks are overlain by high-velocity rocks and underlain by slower-velocity rocks, which also make up the core of the dome (Figure 11a). Despite the wide-azimuth high-density blended acquisition, with offsets up to 10 km, the near-offset coverage is still poor. The lack of recorded offsets makes it difficult to obtain a reasonable velocity model with conventional ray-based tomography methods because there is little to no reliable moveout information and inadequate angle and offset distributions at shallow depths. Moreover, the presence of strong velocity inversions is difficult to capture with first-break inversion methods.

MWI was used for this data set to obtain an accurate estimate of the near-subsurface model by jointly inverting surface-wave dispersion curves and first-break picks up to a maximum 1 km offset. The unsupervised ML approach presented previously was used to create a surface-wave guide to ease and improve the picking of dispersion curves on the full volume. Even with a minimum sweep frequency of 1.5 Hz, the presence of scattering noise from

the complex near surface made it difficult to achieve reliable surface-wave picks below 2.5 Hz with deblended (active) data. However, the picking of the first breaks and surface waves above 2.5 Hz gave a detailed MWI near-surface model, capturing the shallow lateral velocity variations, albeit with a lack of depth penetration 150 m below the topography. The blended continuous recordings were then used to reconstruct ultra-low-frequency surface waves through interferometry, as presented in the previous section. These virtual shots enabled reliable picking of dispersion curves with minimum frequencies as low as 1.2 Hz, and therefore the penetration depth for the MWI can reach approximately 400 m below the surface. In Figure 11, we co-render the legacy velocity model with the Kirchhoff-migrated image for a depth slice at 200 m below the surface (Figure 11a) and two vertical sections within the area (Figures 11b and 11c). A general trend of spatial near-surface velocity variation is captured by the legacy model. However, the velocity update obtained by MWI, with the combined use of surface-wave dispersion curves from active and virtual data, resulted in a much more detailed near-surface V_P model (Figure 11d).

Because the MWI accurately captures the high velocity overlying the dipping flanks of the thrust and the underlying low velocity (black arrows in Figure 11f), it significantly improves structural definition of the thrust fault (black arrows in Figure 11d) and depth positions of the near-surface reflectors (Figures 11e and 11f). As observed with the previous case study, more detailed near-surface velocity models not only improve the images at shallow depth (within the dashed blue box in Figure 12e), they also have a positive impact on the deeper imaging, as shown in Figures 12d and 12e, where the continuity of the deep events (within the dashed blue circle) below the thrust area is improved. It should be noted that, for these examples, the MWI model was merged with the legacy velocity model from approximately 400 m below the surface. Finally, by

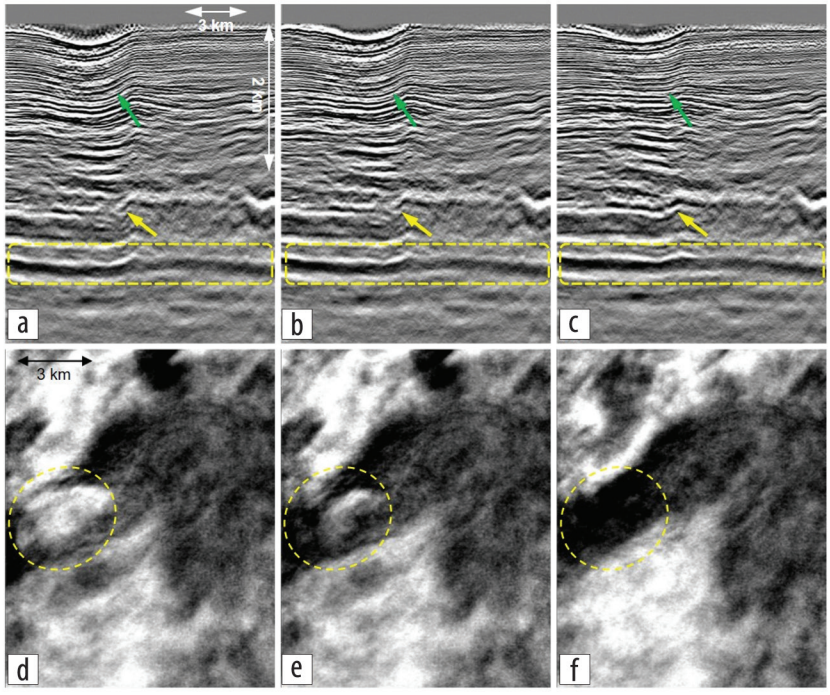

Figure 10. Top: Kirchhoff depth-migrated sections with the (a) legacy tomography-based velocity model, (b) MWI model from active data merged with the legacy model, and (c) MWI model from active and virtual data merged with the legacy model. The green and yellow arrows indicate areas of improved focusing and simpler structures below the wadi. The yellow dashed squares indicate the location of the depth slices. Bottom: Kirchhoff depth-migrated slice at 3.6 km with the (d) legacy tomography-based velocity model, (e) MWI model from active data merged with the legacy model, and (f) MWI model from active and virtual data merged with the legacy model. The yellow circles indicate the location of the wadi.

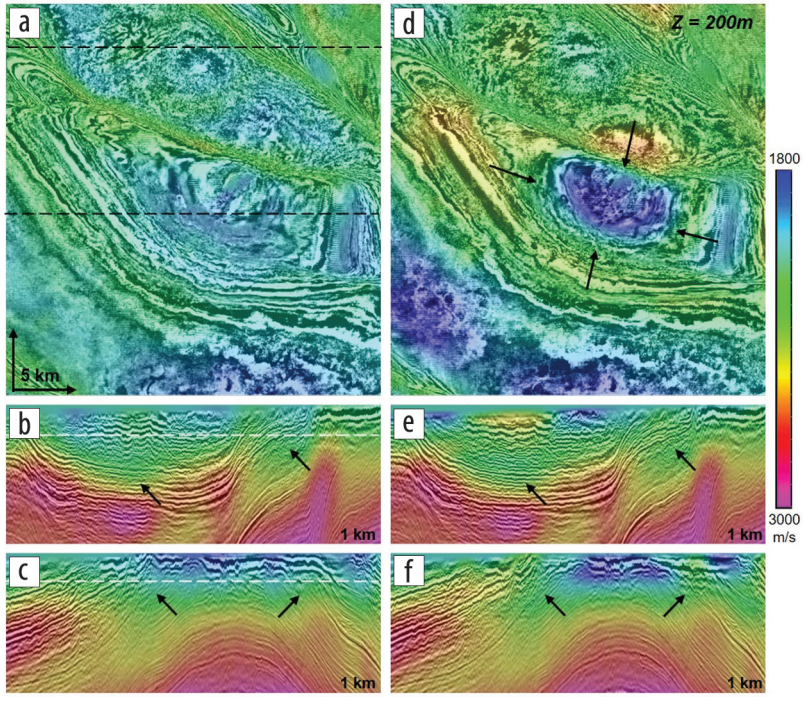

Figure 11. Depth slice (200 m below the topography) and inline sections of Kirchhoff depth migrations (a–c) with velocity overlaid for the legacy model and (d–f) with active and virtual MWI merged with the legacy model. Note the structurally improved image of the dipping areas/crestal structure and slow/fast velocity details in the very shallow part of the section (black arrows).

comparing the snail gather (common offset and azimuth) shown in Figures 12c and 12f, the improvements in gather residual moveout flatness are clearly visible, which enables better residual curvature picking at larger offsets for conventional traveltime tomography. The near-surface model obtained with this advanced workflow can also benefit the subsequent model-building steps, such as full-waveform inversion, thanks to a more accurate shallow input velocity model (Masclet et al., 2020).

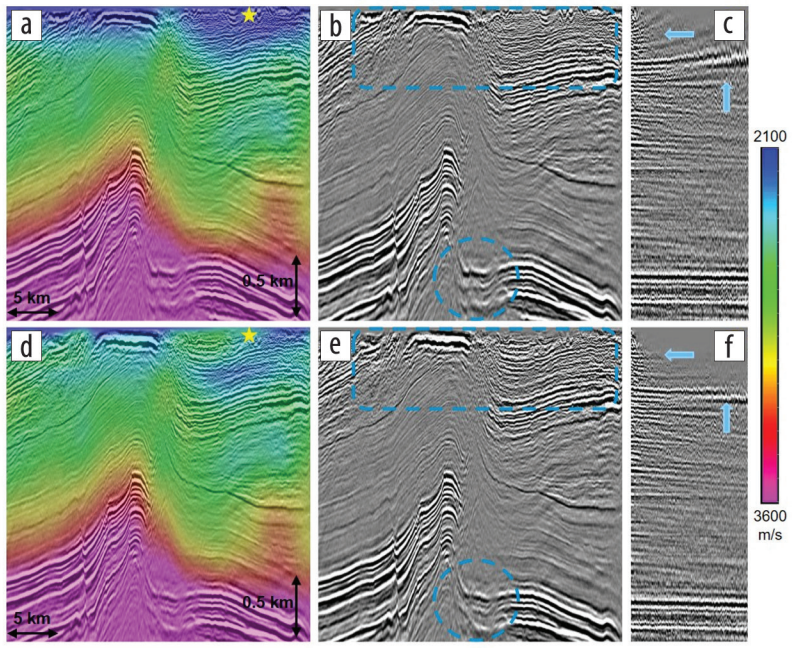

Figure 12. Comparison of (a) the legacy velocity model, (b) its corresponding Kirchhoff-migrated image, and (c) snail common-image gather, with (d) active and virtual data MWI model merged with the legacy one at 400 m below the topography, (e) its corresponding Kirchhoff-migrated image, and (f) snail common-image gather. The yellow stars indicate the location of the common-image gathers. The blue squares, circles, and arrows indicate areas of improved image focusing in the shallow and deeper parts of the section.

Conclusions

MWI is a key technology for improved depth velocity model building using land data from the Middle East. The main success factors are: (1) an unsupervised machine learning approach to build a guide for more precise estimation of vertical and lateral velocity variations in surface waves in different geologic settings and (2) the use of ultra-low-frequency surface waves that allow a near-surface velocity update down to a depth of several hundred meters below the surface. This deeper penetration enables the capture of shallow velocity inversions, which are usually challenging to capture with either first-break tomography or low-frequency FWI. From the two different examples shown, we demonstrated that by incorporating a shallow MWI model update into the depth velocity model, the resulting seismic depth image is significantly improved and more geologically interpretable. Moreover, by improving common-image gather quality, this method is beneficial for subsequent updates of the deeper velocity model. The near-surface P- and S-wave velocity models obtained from MWI can also be used as input shallow models for elastic FWI. TLE

Acknowledgments

We would like to thank Petroleum Development Oman and the Ministry of Energy and Minerals of the Sultanate of Oman for permission to publish the data examples. We also thank all of our colleagues who helped with this project and CGG for permission to publish this work.

Data and materials availability

Data associated with this research are confidential and cannot be released.

Corresponding author: daniela.donno@cgg.com

References

Abma, R., D. Howe, M. Foster, I. Ahmed, M. Tanis, Q. Zhang, A. Arogunmati, and G. Alexander, 2015, Independent simultaneous source acquisition and processing: Geophysics, **80**, no. 6, WD37–WD44, https://doi.org/10.1190/geo2015-0078.1.

Al-Droushi, O., Q. Al-Siyabi, B. Al-Adawi, A. Adwani, M. Danilouchkine, F. ten Kroode, and F. Ernst, 2021, Ambient noise seismic interferometry — Two case studies in Sultanate of Oman: Presented at the Challenges and New Advances in Velocity Model Building Workshop, SEG and DGS.

Bardainne, T., 2018, Joint inversion of refracted P-waves, surface waves and reflectivity: 80th Conference and Exhibition, EAGE, Extended Abstracts, https://doi.org/10.3997/2214-4609.201801158.

Boiero, D., E. Wiarda, and P. Vermeer, 2013, Surface- and guided-wave inversion for near-surface modeling in land and shallow marine seismic data: The Leading Edge, **32**, no. 6, 638–646, https://doi.org/10.1190/tle32060638.1.

Boué, A., R. Courbis, M. Chmiel, N. Arndt, T. Lecocq, A. Mordret, P. Boué et al., 2019, V_S imaging from ambient noise Rayleigh wave tomography for oil exploration in Nevada, USA: 89th Annual International Meeting, SEG, Expanded Abstracts, 5382–5385, https://doi.org/10.1190/segam2019-w21-01.1.

Bouhdiche, O., L. Vivin, P. Plasterie, T. Rebert, M. Retailleau, D. Le Meur, and A. El-Emam, 2020, Multi-wave inversion for near-surface velocity model building on a broadband land survey in North Kuwait: 82nd Conference and Exhibition, EAGE, Extended Abstracts, https://doi.org/10.3997/2214-4609.202011061.

Brenguier, F., A. Mordret, R. Lynch, R. Courbis, X. Campbell, P. Boué, M. Chmiel et al., 2019, Monitoring of fields using body and surface waves reconstructed from passive seismic ambient noise: 89th Annual International Meeting, SEG, Expanded Abstracts, 3036–3040, https://doi.org/10.1190/segam2019-3216217.1.

Chiffot C., A. Prescott, M. Grimshaw, F. Oggioni, M. Kowalczyk-Kedzierska, S. Cooper, D. Le Meur, and R. Johnston, 2017, Data-driven interferometry method to remove spatially aliased and nonlinear surface waves: 87th Annual International Meeting, SEG, Expanded Abstracts, 4980–4985, https://doi.org/10.1190/segam2017-17724305.1.

Colombo, D., M. Cogan, S. Hallinan, M. Mantovani, M. Virgilio, and W. Soyer, 2008, Near-surface P-velocity modelling by integrated seismic, EM and gravity data: Examples from the Middle East: First Break, **26**, no. 10, https://doi.org/10.3997/1365-2397.26.10.28560.

Dal Moro, G., and M. Pipan, 2007, Joint inversion of surface wave dispersion curves and reflection travel times via multi-objective evolutionary algorithms: Journal of Applied Geophysics, **61**, no. 1, 56–81, https://doi.org/10.1016/j.jappgeo.2006.04.001.

Dellinger, J. A., and J. Yu, 2009, Low-frequency virtual point-source interferometry using conventional sensors: 71st Conference and Exhibition, EAGE, Extended Abstracts, https://doi.org/10.3997/2214-4609.201400529.

Duret, F., F. Bertin, K. Garceran, R. Sternfels, T. Bardainne, N. Deladerriere, and D. Le Meur, 2016, Near-surface velocity modeling using a combined inversion of surface and refracted P-waves: The Leading Edge, **35**, no. 11, 946–951, https://doi.org/10.1190/tle35110946.1.

Forbes, G. A., H. S. M. Jansen, and J. Schreurs, 2010, Lexicon of Oman: Subsurface stratigraphy: Reference guide to the stratigraphy of Oman's hydrocarbon basins: GeoArabia Special Publication.

Golikov, P., and A. Bakulin, 2014, Building near-surface models with velocity inversions and evaluating their impact on depth imaging: 84th Annual International Meeting, SEG, Expanded Abstracts, 3508–3512, https://doi.org/10.1190/segam2014-0703.1.

Hou, S., S. Angio, H. Hoeber, V. Massart, L. Peng, R. Johnston, and R. Walters, 2019, Application of unsupervised machine learning to the processing of a land mega-survey: Subsurface Intelligence Workshop, EAGE, Extended Abstracts, https://doi.org/10.3997/2214-4609.2019X6104.

Le Meur, D., D. Donno, J. Courbin, D. Solyga, and A. Prescott, 2020, Retrieving ultra-low frequency surface waves from land blended continuous recording data: 90th Annual International Meeting, SEG, Expanded Abstracts, 1855–1859, https://doi.org/10.1190/segam2020-3418624.1.

MacQueen, J., 1967, Some methods for classification and analysis of multivariate observations: Proceedings of the Berkeley Symposium on Mathematical Statistics and Probability, **1**, 281–297.

Masclet, S., T. Bardainne, V. Massart, and H. Prigent, 2019, Near surface characterization in Southern Oman: Multi-wave inversion guided by machine learning: 81st Conference and Exhibition, EAGE, Extended Abstracts, https://doi.org/10.3997/2214-4609.201900968.

Masclet, S., G. Bouquard, and H. Prigent, 2020, Multi-wave and full-waveform inversion in Southern Oman: 82nd Conference and Exhibition, EAGE, Extended Abstracts, https://doi.org/10.3997/2214-4609.202010731.

Pérez Solano, C., and R. E. Plessix, 2019, Velocity-model building with enhanced shallow resolution using elastic waveform inversion — An example from onshore Oman: Geophysics, **84**, no. 6, R977–R988, https://doi.org/10.1190/geo2018-0736.1.

Prieux, V., T. Bardainne, A. Meffre, H. Prigent, F. J. Van Kleef, M. Waqas, and L. Hou, 2020, Structurally constrained anisotropic multi-wave-inversion utilizing machine learning and big data on a Middle East OBC project: 82nd Conference and Exhibition, EAGE, Extended Abstracts, https://doi.org/10.3997/2214-4609.202011047.

Re, S., C. Strobbia, M. De Stefano, and M. Virgilio, 2010, Simultaneous joint inversion of the refracted and surface waves: 80th Annual International Meeting, SEG, Expanded Abstracts, 1914–1918, https://doi.org/10.1190/1.3513216.

Schuster, G. T., 2009, Seismic interferometry: Cambridge University Press, https://doi.org/10.1017/CBO9780511581557.

Sedova, A., G. Royle, O. Hermant, M. Retailleau, and G. Lambaré, 2017, High-resolution land full waveform inversion: A case study on a data set from the Sultanate of Oman: 79th Conference and Exhibition, EAGE, Extended Abstracts, https://doi.org/10.3997/2214-4609.201701163.

Snieder, R., 2004, Extracting the Green's function from the correlation of coda waves: A derivation based on stationary phase: Physical Review E, **69**, no. 4, https://doi.org/10.1103/PhysRevE.69.046610.

Socco, L. V., and C. Strobbia, 2004, Surface-wave method for near-surface characterization: A tutorial: Near Surface Geophysics, **2**, no. 4, 165–185, https://doi.org/10.3997/1873-0604.2004015.

Sternfels, R., G. Viguier, R. Gondoin, and D. Le Meur, 2015, Joint low-rank and sparse inversion for multidimensional simultaneous random/erratic noise attenuation and interpolation: 77th Conference and Exhibition, EAGE, Extended Abstracts, https://doi.org/10.3997/2214-4609.201412979.

Stopin, A., S. Abri, and R. E. Plessix, 2013, Waveform inversion of a large low-frequency wide-azimuth land data set in Oman: 75th Conference and Exhibition, EAGE, Extended Abstracts, https://doi.org/10.3997/2214-4609.20130832.

Strobbia, C., and S. Foti, 2006, Multi-offset phase analysis of surface wave data (MOPA): Journal of Applied Geophysics, **59**, no. 4, 300–313, https://doi.org/10.1016/j.jappgeo.2005.10.009.

Taillandier, C., M. Noble, H. Chauris, and H. Calandra, 2009, First arrival traveltime tomography based on the adjoint-state method: Geophysics, **74**, no. 6, WCB1–WCB10, https://doi.org/10.1190/1.3250266.

Wapenaar, K., 2004, Retrieving the elastodynamic Green's function of an arbitrary inhomogeneous medium by cross correlation: Physical Review Letters, **93**, no. 25, https://doi.org/10.1103/PhysRevLett.93.254301.

Zhao, J., H. Jin, Y. Zhu, Y. C. El-Taha, and F. Clow, 2018, Vibroseis ultra high productivity blended acquisition: Field trial and full-scale implementation in Oman: 88th Annual International Meeting, SEG, Expanded Abstracts, 150–153, https://doi.org/10.1190/IGC2018-038.